Solar Physics (2006) 234: 273–299
DOI: 10.1007/s11207-006-0093-6

SHRINKING AND COOLING OF FLARE LOOPS IN A TWO-RIBBON FLARE

BOJAN VRŠNAK and MANUELA TEMMER
Hvar Observatory, Faculty of Geodesy, Zagreb, Croatia
`(e-mails: bvrsnak@geodet.geof.hr; mat@igam.uni-graz.at)`

ASTRID VERONIG
IGAM/Institute of Physics, University of Graz, Graz, Austria
`(e-mail: asv@igam.uni-graz.at)`

MARIAN KARLICKÝ
Astronomical Institute of the Academy of Sciences of the Czech Republic, Ondřejov, Czech Republic
`(e-mail: karlicky@asu.cas.cz)`

and

JUN LIN
Yunnan Astronomical Observatory, Chinese Academy of Sciences, Kunming, Yunnan, P.R. China
and Harvard-Smithsonian Center for Astrophysics, Cambridge, Massachusetts, U.S.A.
`(e-mail: jlin@ynao.ac.cn, jlin@cfa.harvard.edu)`

(Received 19 October 2005; accepted 20 December 2005)

Abstract. We analyze the evolution of the flare/postflare-loop system in the two-ribbon flare of November 3, 2003, utilizing multi-wavelength observations that cover the temperature range from several tens of MK down to 10^4 K. A non-uniform growth of the loop system enables us to identify analogous patterns in the height–time, $h(t)$, curves measured at different temperatures. The "knees," "plateaus," and "bends" in a higher-temperature curve appear after a certain time delay at lower heights in a lower-temperature curve. We interpret such a shifted replication as a track of a given set of loops (reconnected field lines) while shrinking and cooling after being released from the reconnection site. Measurements of the height/time shifts between $h(t)$ curves of different temperatures provide a simultaneous estimate of the shrinkage speed and cooling rate in a given temperature domain, for a period of almost ten hours after the flare impulsive phase. From the analysis we find the following: (a) Loop shrinkage is faster at higher temperatures – in the first hour of the loop-system growth, the shrinkage velocity at 5 MK is 20 – 30 km s^{-1}, whereas at 1 MK it amounts to 5 km s^{-1}; (b) Shrinking becomes slower as the flare decays – ten hours after the impulsive phase, the shrinkage velocity at 5 MK becomes 5 km s^{-1}; (c) The cooling rate decreases as the flare decays – in the 5 MK range it is 1 MK min^{-1} in the first hour of the loop-system growth, whereas ten hours later it decreases to 0.2 MK min^{-1}; (d) During the initial phase of the loop-system growth, the cooling rate is larger at higher temperatures, whereas in the late phases the cooling rate apparently does not depend on the temperature; (e) A more detailed analysis of shrinking/cooling around one hour after the impulsive phase reveals a deceleration of the loop shrinkage, amounting to $\bar{a} \approx 10\,\mathrm{m\,s^{-2}}$ in the $T < 5$ MK range; (f) In the same interval, conductive cooling dominates down to $T \approx 3$ MK, whereas radiation becomes dominant below $T \approx 2$ MK; (g) A few hours after the impulsive phase, radiation becomes dominant across the whole $T < 5$ MK range. These findings are compared with results of previous studies and discussed in the framework of relevant models.

1. Introduction

A two-ribbon flare (or dynamical flare; Švestka, 1986) is a consequence of fast reconnection of the magnetic field in the current sheet formed in the wake of a coronal mass ejection (CME). The CME stretches vertically the bipolar magnetic field present in the pre-erupting structure, so the current sheet forms between oppositely directed field lines emanating from the two sides of the photospheric magnetic field inversion line (*e.g.*, Ko *et al.*, 2003; Webb *et al.*, 2003; Lin *et al.*, 2005). In the course of the eruption, the current sheet elongates and when the length-to-width ratio becomes large enough the tearing instability sets in, resulting in fast reconnection of the magnetic field (*e.g.*, Furtsh, Kileen, and Rosenbluth, 1963; Ugai, 1987; Gekelman and Pfister, 1988; and Vršnak *et al.*, 2003, for analytical, numerical, experimental, and observational results, respectively).

After the onset of fast reconnection, the highly bent reconnected field lines are expelled along the current sheet by the sling-shot effect of the magnetic tension. Upward and downward outflow jets of hot plasma are formed, carrying away the reconnected field. The downward jet is restricted to the space between the reconnection site and the solar surface. After leaving the current sheet, the plasma flow decelerates, creating a deflection sheath (Forbes, 1986) in which the field-line loops are compressed due to decelerated shrinking (*e.g.*, Karlický, Veronig, and Vršnak, 2005).

The idea of loop shrinkage was put forward by Švestka *et al.* (1987) who noted that in a growing flare/postflare loop system, cool loops never reach the height of hot loops, and interpreted this as a consequence of shrinking. After Švestka *et al.* (1987), several observational and theoretical studies were performed to demonstrate this motion (Hiei, 1994; Lin *et al.*, 1995; Forbes and Acton, 1996; Lin, 2004; Sheeley, Warren, and Wang, 2004; Li and Gan, 2005). Also relevant in this respect are observations presented by McKenzie (2000), McKenzie and Hudson (1999), Innes, McKenzie, and Wang (2003), which reveal downward flows in flare-associated hot coronal structures.

In the course of shrinking, the plasma confined within a given loop cools due to conductive and radiative losses. The final state is a stationary loop cooled to chromospheric temperature, usually observed as the Hα postflare loop.

Cooling of flare loops was studied by a number of authors (*e.g.*, Švestka, 1987; Švestka *et al.*, 1987; Culhane *et al.*, 1994; Schmieder *et al.*, 1996; van Driel-Gesztelyi *et al.*, 1996; Varady and Heinzel, 1997a,b; Aschwanden and Alexander, 2001, and references therein). It is generally accepted that conductive cooling dominates at high temperatures, whereas radiation becomes dominant at lower temperatures. However, the details strongly depend on the plasma density and loop length (Varady and Heinzel, 1997b), the evaporation process (Antiochos and Sturrock, 1978), heating processes associated with the shrinking/compression (Karlický, Veronig, and Vršnak, 2005), and details of the loop geometry (Dowdy, Moore, and Wu, 1985).

In this paper, we present an analysis of multi-wavelength observations of the growing loop system of the X3.9 flare that occurred on November 3, 2003, covering a time interval of almost ten hours. These measurements enable us to analyze the shrinking and cooling of flare loops from the impulsive phase up to the late post-impulsive phase of the flare. In Sections 2 and 3 we describe the observations, explain the method, and present the measurements. The main results are given in Sections 4 and 5, and are discussed in Section 6. In Appendices A and B, we present some additional observational details.

2. Observations

2.1. INSTRUMENTS

In the following analysis, we use data from several ground-based and space-borne instruments, covering the temperature range of more than three orders of magnitude, from 10^4 to $>10^7$ K.

The hottest component of the flare loop system, observed as the hard X-ray loop-top source (Liu *et al.*, 2004; Veronig *et al.*, 2005), was recorded by the Ramaty High Energy Solar Spectroscopic Imager (RHESSI). RHESSI is a NASA Small Explorer Mission designed to study high energy solar flare emission with high spectral and spatial resolution (Lin *et al.*, 2002). For the present analysis, we studied time sequences of RHESSI images in the 10 – 15 and 25 – 30 keV energy bands reconstructed with the CLEAN algorithm (Hurford *et al.*, 2002) using detectors 3 – 8, which give a FWHM angular resolution of ~7 arcsec. The integration time of each image is 16.2 seconds; the pixel resolution is 1 arcsec (for details see Veronig *et al.*, 2005). The RHESSI instrument is particularly sensitive to flare plasmas in excess of 10 MK.

In soft X-rays (SXR) the flare loop system was observed by the Soft X-ray Imager[1] (SXI; Hill *et al.*, 2005; Pizzo *et al.*, 2005) onboard the GOES 12 spacecraft. The maximum sensitivity of SXI is primarily in the temperature range 1 – 10 MK. For the loop-top position measurements we used four different SXI analysis filters sensitive to different temperatures: open filter position (2.9 – 3.4 MK; hereafter SXI-o), the thin polyimide filter (3.8 MK; hereafter SXI-pt), the medium polyimide filter (3.8 – 4.0 MK; hereafter SXI-pm), and the thin beryllium filter (5 MK; hereafter SXI-b). The spatial resolution of SXI images is 5 arcsec/pixel.

The loops at quiet-coronal temperatures were measured in the EUV-range utilizing Fe XII 195 Å images obtained by the Extreme-ultraviolet Imaging Telescope[2] (EIT; Delaboudinière *et al.*, 1995) onboard the Solar and Heliospheric Observatory (SOHO). This channel shows coronal structures at temperatures around 1.6 MK. The images have a resolution of 2.6 arcsec/pixel, and a field-of-view extending to 1.4 solar radii.

[1] `http://sxi.ngdc.noaa.gov/`

[2] `http://umbra.nascom.nasa.gov/eit/`

The growth of the cool postflare loop system is traced utilizing Hα observations from the Kanzelhöhe Solar Observatory (KSO), Austria (Otruba, 1999; Otruba and Pötzi, 2003). KSO routinely takes full-disk Hα images with a time cadence of $\sim$ five seconds and a spatial resolution of 2.2 arcsec/pixel. When the flare mode is triggered, additional images in the blue and red wing of the Hα spectral line (at the off-band center wavelength of H$\alpha - 0.3$ Å and H$\alpha + 0.4$ Å) are taken with a cadence of about one image per minute in each wing. In Hα, we see plasma at temperatures of about 10^4 K (*e.g.*, Švestka, 1976; Heinzel and Karlický, 1987).

For the comparative study of the loop-top evolution in different wavelengths, it was necessary to accurately co-align all imaged data sets. We co-aligned the Hα flare images with the RHESSI flare images based on the two footpoints seen in both hard X-rays and Hα for different times of the flare evolution. We found that the Hα images were offset with respect to the RHESSI images by -2 arcsec in x and $+8$ arcsec in y. After this correction, the Hα footpoints turned out to be also co-spatial (to the accuracy of the spatial resolution of the EIT and Hα images of $2-3$ arcsec) with the footpoint regions inferred from EIT images. This implies that RHESSI and EIT are co-aligned as they are. The SXI images were co-aligned comparing SXI and EIT pre-flare images of active regions with the result that SXI was offset with regard to EIT by -16 arcsec in x and $+4$ arcsec in y. Note that the uncertainties are largest in SXI, which has a resolution of 5 arcsec/pixel.

2.2. FLARE EVOLUTION

The two-ribbon X3.9 flare of November 3, 2003 was centered at N08W77, at the northern edge of the active region NOAA 10488 (Figure 1). The GOES $1-8$ Å burst started around 09:43 UT and attained a double maximum at 09:54/10:02 UT. Detailed descriptions of the flare morphology and the energy release evolution based on the X-ray observations are presented by Liu *et al.* (2004) and Veronig *et al.* (2005), whereas Dauphin *et al.* (2005) analyzed the flare-associated type IV radio emission. The flare occurred in conjunction with a fast CME ($v \approx 1400\,\mathrm{km\,s^{-1}}$), heading along position angle PA $\approx 300^\circ$. The back-extrapolation of the CME trajectory indicates the take-off occurred between 09:40 and 09:55 UT. The flare/CME event launched a large-scale coronal wave, which caused a Moreton wave and a complex type II burst (Vršnak *et al.*, 2005, 2006).

The development of the flare loop system started by the downward motion of the X-ray loop-top source observed by RHESSI (Liu *et al.*, 2004; Veronig *et al.*, 2005). This phase lasted from 09:46:00 to 09:48:30 UT and was studied in detail and interpreted in terms of a collapsing magnetic trap by Veronig *et al.* (2005) and Karlický, Veronig, and Vršnak (2005). In the following, we analyze only the loop-system growth, starting at 09:49 UT.

In Figure 1 we show the appearance of the loop system observed by RHESSI, SXI, EIT, and KSO-Hα instruments. EIT observed an arcade of loops, and several

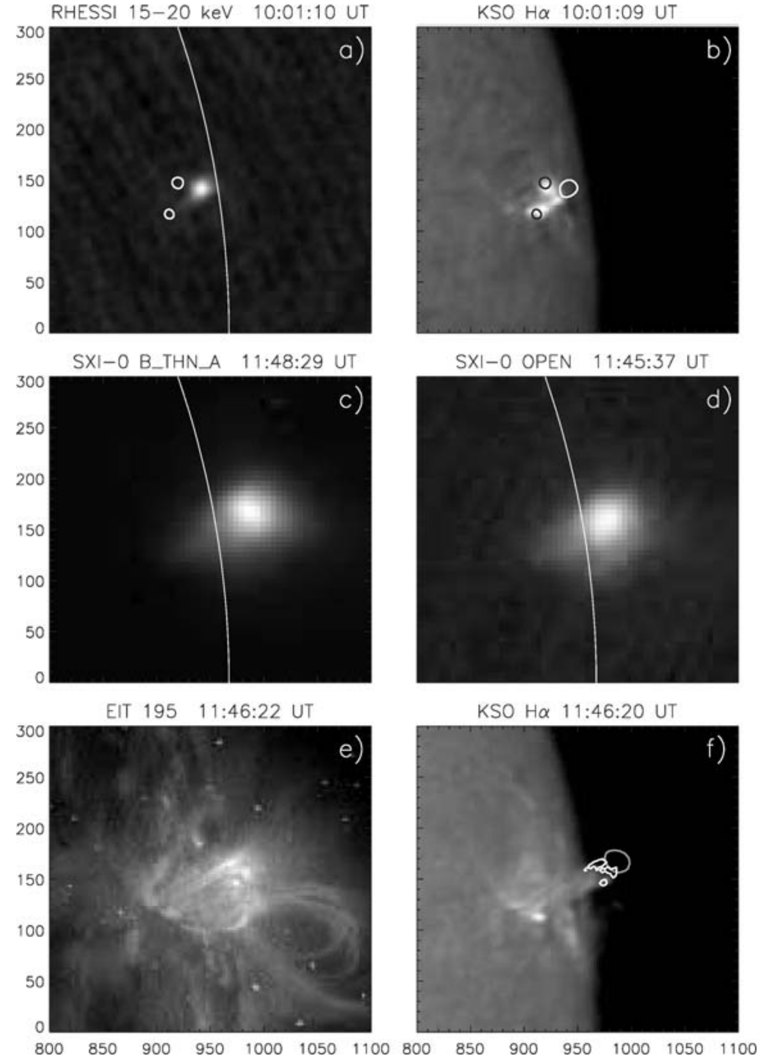

Figure 1. Images of the loop-top (LT) source observed in different wavelengths. Panels (a) and (b) are taken approximately at the same time during the impulsive phase around 10:01 UT. Panels (c) – (f) are taken from the flare decay phase, around 10:46 UT. (a) RHESSI 15 – 20 keV image of the LT source; overlayed are the 50% contours from the RHESSI footpoint sources (FP) reconstructed in the 70 – 100 keV energy band. (b) KSO-Hα image, overlayed are the RHESSI FPs (*black contour*, 50% level) and LT source (*white contour*, 50% level). (c) SXI image, thin beryllium filter. (d) SXI image, open filter position. (e) EIT 195 Å image. (f) KSO-Hα image; overlayed are the EIT (*white contours*, 50% level) and the SXI thin beryllium filter image (*gray contours*, 75% level) shown in panels (e) and (c), respectively.

individual loops could be distinguished in Hα. SXI only saw a bright blob probably because of the lower spatial resolution of 10 arcsec FWHM (5 arcsec/pixel) compared to the EIT 2.6 arcsec/pixel and Hα 2.2 arcsec/pixel. Note that in EIT no measurements could be performed before 11:00 UT, since the EIT detectors were saturated.

2.3. MEASUREMENTS OF THE LOOP-SYSTEM GROWTH

The growth of the loop system is quantified by measuring the plane-of-sky distances, $h(t)$, of the loop-top sources along the main axis of the loop system (Figure 1). The axis was determined by a linear fit to the loop-top centroid data independently for the Hα, EIT, SXI, and RHESSI image sequences: The loop-system axis turned out to be inclined 15 – 19° north from the radial direction (for details see Veronig *et al.*, 2005), consistent with the non-radial component of the CME motion (Vršnak *et al.*, 2006). The intersection of the main axis of the system and the line connecting the RHESSI footpoint sources is used as the point from which the distance (h) was measured.

In Figure 2 we present the complete set of the $h(t)$ measurements of the flare loop-system evolution. The time (t) is expressed in minutes after 09:40 UT. In the inset, the first hour of the loop-system growth is enlarged. The inset presents the initial downward motion of the X-ray loop-top sources which was studied by Liu *et al.* (2004) and Veronig *et al.* (2005). In the following, we focus on the phase of the loop-system growth, starting around the peak of the HXR burst, 09:49 – 09:50 UT.

2.4. OVERALL CHARACTERISTICS OF THE LOOP-SYSTEM GROWTH

At 09:49 UT the RHESSI loop-top source was at the lowest height, corresponding to a plane-of-sky distance $h = 7 – 8$ Mm (Figure 3a). Its rise-velocity during the first HXR impulsive peak amounted to $\mathrm{d}h/\mathrm{d}t \approx 40\,\mathrm{km\,s^{-1}}$. In the same interval, the RHESSI footpoint kernels were expanding away from the neutral line with a plane-of-sky velocity $\approx 25\,\mathrm{km\,s^{-1}}$. A similar velocity is found for the expansion of the Hα ribbons (see the inset in Figure 3a, dashed line). Taking into account the foreshortening, one finds the true expansion velocity was in the range $35 – 40\,\mathrm{km\,s^{-1}}$, which is quite similar to the RHESSI loop-top rise-velocity.

The Hα postflare loops became recognizable around 10 UT, *i.e.*, some ten minutes after the HXR impulsive peak (Figures 2 and 3a). In the first half-hour interval, the growth rate, estimated from the smoothed $h(t)$ data, was fluctuating between five and ten $\mathrm{km\,s^{-1}}$. The measurements of the Hα loops could be measured in the KSO filtergrams until 12:30 UT, when the loops became too faint to be measured. However, the long-exposure Hα images from the Rimavska Sobota Observatory (Slovakia) reveal that the Hα loop system was still growing at $\approx$ 1500 UT (when their observations ended), which is more than five hours after the impulsive phase.

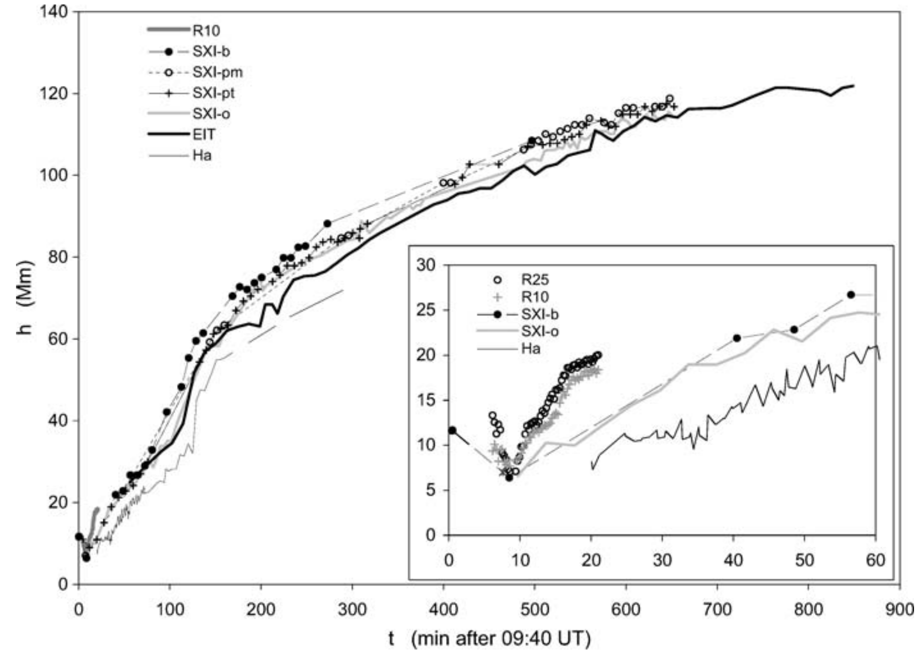

Figure 2. Growth of the flare/postflare loop system. R10: RHESSI 10 – 15 keV; SXI-b: thin beryllium filter; SXI-pm: medium polyimide filter; SXI-pt: thin polyimide filter; SXI-o: open filter position; EIT: EIT 195 Å; Ha: KSO-Hα (for details see Section 2.1). The time is expressed in minutes after 09:40 UT. In the inset, the first one-hour interval is enlarged, showing also the RHESSI 25 – 30 keV source (R25).

The growth of the EIT postflare loop system could be measured over more than 14 hours. At the end of the day, the EIT loops grew at a velocity of $v_{\mathrm{EIT}} = 0.5\ \mathrm{km\ s^{-1}}$.

Figures 1 – 3 reveal a clear structuring with temperature, *i.e.*, higher temperature plasma is located above lower temperature plasma.

3. The Data Analysis

3.1. THE METHOD

Figures 2 and 3 show that the loop-system growth ($\mathrm{d}h/\mathrm{d}t$) was changing in time. Inspecting the growth of the system in various energy channels, one finds that some characteristic features (“knees,” “bends,” “plateaus”) are repeated in two or more neighboring curves. All of these features are shifted in height (Δh) and time (Δt) in such a manner that the cooler signature appears at a lower height with a certain time delay. Our working hypothesis is that such duplicated elements reveal the same set of field lines (loops) at different temperatures.

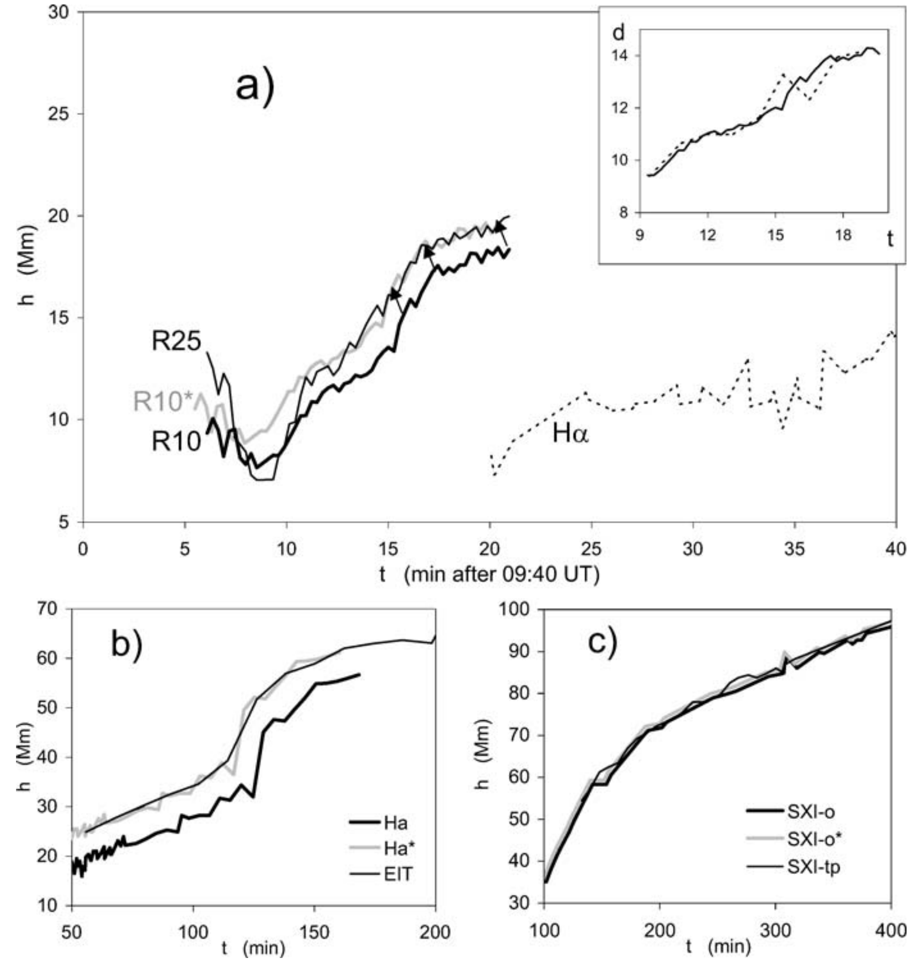

Figure 3. Overlapping of corresponding elements in $h(t)$ curves of different temperatures. *Black lines* are the original $h(t)$ measurements, whereas the *gray lines* show the lower temperature curves shifted by Δh and Δt to overlap the corresponding element of the higher temperature curve. Symbols R25 and R10 given in the legend denote RHESSI 25 – 30 and 10 – 15 keV bands, respectively. The fluctuations in the curves give an information on the measurement uncertainties. (a) Overlapping R10 → R25 at $t = 15 – 20$ minutes $\Delta h = 1.2$ Mm and $\Delta t = 0.6$ min, at $\langle t \rangle = 17.5$ min; the initial phase of Hα loop growth is also shown as a reference. (b) Overlapping H$\alpha \rightarrow$ EIT at $t = 100 – 150$ min: $\Delta h = 4.5$ Mm and $\Delta t =$ eight minutes, at $\langle t \rangle = 125$ min and $\langle T \rangle = 0.8$ MK. (c) Overlapping SXI-o → SXI-pt at $t = 150 – 300$ min: $\Delta h = 1$ Mm and $\Delta t = 2$ min, at $\langle t \rangle = 225$ min and $\langle T \rangle = 3.4$ MK. In the inset of panel (a) we show the expansion of Hα flare ribbons (*dashed line*) compared with the RHESSI 10 – 15 keV loop-top height (*solid line*, shifted and scaled to overlap the ribbon data).

Changes of the loop-system growth rate could be caused by two effects. First, they could be related to the reconnection process. For example, the rate by which field lines are detached (released) from the current sheet may vary in time. Consequently, the growth of the system would not be constant, since the rate at which

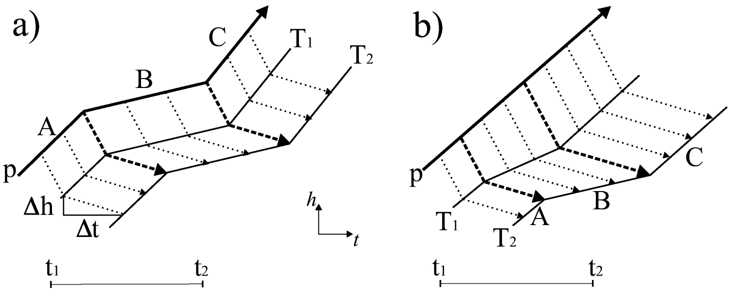

Figure 4. Sketch of changes in the loop-system growth rate due to (a) changing flux release rate at constant shrinkage and cooling characteristics; (b) changing cooling characteristics at constant release rate. The p-line depicts the rise $h(t)$ of the lower edge of the current sheet. *Dotted arrows* outline the shrinkage/cooling process to the temperature T_1 and then to T_2. The "knees" between phases A and B and the bends between B and C are connected by *bold-dashed arrows*.

the magnetic flux is transported ($\mathbf{v}_o \times \mathbf{B}_o$) downwards by the reconnection outflow is changing (for details see Section 5.1 of Veronig *et al.*, 2005). In other words, such changes are basically related to variations of the reconnection rate, *i.e.*, by the magnetic flux inflow into the current sheet ($\mathbf{v}_i \times \mathbf{B}_i$). Another possibility is that the "release rate" is the same but the cooling/shrinking process changes. In both cases, a particular change of the loop-system growth rate observed at temperature T_1, and then after Δt at a lower temperature $T_2 = T_1 - \Delta T$, is associated with the same set of field lines (Figure 4). Therefore, the measurement of the time and height "shifts," Δt and Δh, between the corresponding elements on two $h(t)$ curves provides an estimate of the related shrinkage speed $v = \Delta h/\Delta t$ and cooling rate $Q = \Delta T/\Delta t$.

In Figure 4a we sketch the growth pattern $h(t)$ associated with variations of the "release rate" at constant cooling and shrinkage rates. In Figure 4b we depict the case of a constant release rate and changing cooling rate. Following the nomenclature used by Lin (2004), the bold line that maps the height of the bottom edge of the currents sheet, $h_p(t)$, is denoted by "p." The rise-velocity $\Delta h_p(t)/\Delta t$ is determined by a number of factors (for details see Lin, 2004), and it is related to the rate at which the field lines are detached from the current sheet ("release rate"). The lines marked by T_1 and T_2 represent the heights of the loop system measured at temperatures T_1 and T_2. The dotted lines connecting the curves p and T_1 show the shrinkage Δh of the field lines during the time Δt needed for the plasma to cool down from the initial temperature to T_1. Analogously, the dotted arrows connecting the curves T_1 and T_2 show the shrinkage during the time needed for cooling from T_1 to T_2. It is assumed that the shrinkage $p \rightarrow T_1$ is faster than $T_1 \rightarrow T_2$, *i.e.*, $v_{p\rightarrow 1} > v_{1\rightarrow 2}$.

In Figure 4a, the release rate temporarily decreases during phase B, which is associated with a slower rise of the "release-height" $h_p(t)$. Consequently, a knee is formed in the p-curve between phases A and B, a plateau during phase B, and a bend between phases B and C. Furthermore, it is assumed that the cooling rate and the shrinkage do not change during the considered interval, so the shape of the p-line is replicated in curves T_1 and T_2. The knees and the bends in the three curves are connected by bold dashed arrows (hereafter "corresponding curve elements").

In Figure 4b we show the situation where the "release point" rises at a constant speed (straight p-line), whereas the cooling rate gradually decreases during phase B (note that successively longer dotted lines connect the p-line with the line T_1, as well as T_1 with T_2).

Let us consider as an example that the $h(t)$ curve measured at the observing temperature T_1 shows a knee, similar to that sketched in Figure 4 at the T_1-curve between segments A and B in the interval $t_1 < t < t_2$. Then, after Δt, an analogous feature is observed in the $h(t)$ curve measured at T_2, shifted by Δh with respect to the height of the "knee" at T_1. In such a case, the shifts Δh and Δt can be used to evaluate the (mean) shrinkage speed $v = \Delta h/\Delta t$ and the (mean) cooling rate $Q = \Delta T/\Delta t$ in the considered time period centered at $\langle t\rangle = (t_1 + t_2)/2$ and the temperature interval centered at $\langle T\rangle = (T_1 + T_2)/2$.

3.2. MEASUREMENTS OF Δh AND Δt

Three characteristic examples of distinct elements in the $h(t)$ curves are shown in Figure 3. We have chosen different examples to demonstrate the diversity of situations we are dealing with. Each situation has some advantages and some drawbacks, leading to a different accuracy of Δh and Δt measurements, *i.e.*, estimates of v and Q.

In Figure 3a we show, by black-bold and black-thin lines, the rise of the loop-top source observed in the RHESSI 10 – 15 and 25 – 30 keV energy bands, respectively (denoted by R10 and R25). Comparing the R25 and R10 curves one finds very similar changes in the growth rate: there is a knee around $t = 11$ min, followed by a period of slower growth in the interval 11 minutes $< t <$ 14 minutes. At $t \approx 15$ minutes the curves bend into the fast growth interval 15 minutes $< t <$ 17 minutes, which is followed by a new knee and a plateau of slower growth. The thin gray line denoted as R10* represents the R10 curve shifted by $\Delta h = 1.2$ Mm and $\Delta t = 0.6$ minutes, giving the best overlap with the R25 curve in the interval 15 minutes $< t <$ 20 minutes. From that one finds the (mean) shrinking velocity $v = \Delta h/\Delta t = 33$ km s^{-1}. Inspecting various combinations of Δh and Δt we find (provisional) upper and lower limit combinations [1.3 Mm; 0.4 min], and [1.1 Mm; 0.7 min], corresponding to $v = 54$ and 26 km s^{-1}, respectively. Unfortunately, from RHESSI measurements we cannot determine the cooling rate, since specifying the temperature separately for the 10 – 15 and 25 – 30 keV sources is quite unreliable. Veronig *et al.* (2005) derived from RHESSI spectroscopy, fitting an isothermal model in the 10 – 30 keV energy range, temperatures in the range 35 – 45 MK, which is indicative of "superhot" plasma (Lin *et al.*, 1981).

In the inset of Figure 3a, we present by the dashed line the expansion of the Hα ribbons away from the magnetic inversion line, $d(t)$. The $d(t)$ behavior is quite similar to the RHESSI loop-top $h(t)$ curve (solid line). We take that as an evidence that the described changes in the $h(t)$ curve are real, rather than being a measurement artifact. Note that such a pattern is indicative of the scenario shown in Figure 4a (at least for the given time span), since the ribbon expansion is directly related to the reconnection rate.

Figure 3b illustrates a situation quite different from that shown in Figure 3a. The bold-black and thin-black curves represent the Hα and EIT measurements, respectively. The time interval involved is considerably longer, covering more than two hours. One finds a very good overall correspondence between the two curves in the period considered. Yet, considering such a long time interval, it should be kept in mind that the slope of the p-curve, or cooling/shrinking characteristics, might undergo an overall systematic change. So, besides determining the overall shift, we also applied separate shifts for the period of slow rise from 60 to 100 minutes, the bend from 100 to 120 minutes, the phase of fast rise from 120 to 140 minutes, and the “gradual knee” from 140 to 170 minutes. In Figure 3b, we show only the overall overlap (120 – 170 minutes) where the Hα curve (thick black) is shifted by 4 Mm and 8 minutes (thick gray). From that one finds a shrinkage velocity of 8 km s^{-1} and a cooling rate of 0.2 MK minute^{-1}. The upper/lower limits are [3 Mm; 10 min], and [5 Mm; 6 min], respectively, which gives $v = 5 – 14$ km s^{-1} and $Q = 0.16 – 0.27$ MK minute^{-1}.

In Figure 3c we present a situation which illustrates the limits of the procedure: the temperature difference between the SXI-o and SXI-pt is only 0.8 MK, so the displacement of the two $h(t)$ curves is comparable to the measurement errors. Furthermore, the change in the $h(t)$ slope is quite gradual, which increases the ambiguity in determining the shifts Δh, Δt. For example, reasonable shifts range from [0.7 Mm; 3 min] to [1 Mm; 1 min]. For the most appropriate shift (hereafter “best overlap”) we take the combination [1 Mm; 2 min] – the SXI-o curve and the shifted SXI-o* curve are shown in Figure 3c by thick-black and thick-gray line, respectively). From these shifts, we find $v = 4 – 17$ km s^{-1} and $Q = 0.27 – 0.80$ MK minute^{-1}, where the most appropriate shift gives $v = 8$ km s^{-1} and $Q = 0.4$ MK minute^{-1}.

4. Results

Applying the procedure explained in Section 3.1 and illustrated in Section 3.2, we determined the shifts for all associable features in all $h(t)$ curve pairs, and from that we evaluated the shrinkage velocities $v = \Delta h/\Delta t$ and cooling rates $Q = \Delta T/\Delta t$ at a given temperature $\langle T\rangle$ and time $\langle t\rangle$.

4.1. COMPLETE DATA SET

In Figure 5, we show the complete set of v and Q measurements as a function of $\langle t\rangle$ and $\langle T\rangle$. The results based on the “best-overlap” shifts are drawn in Figure 5

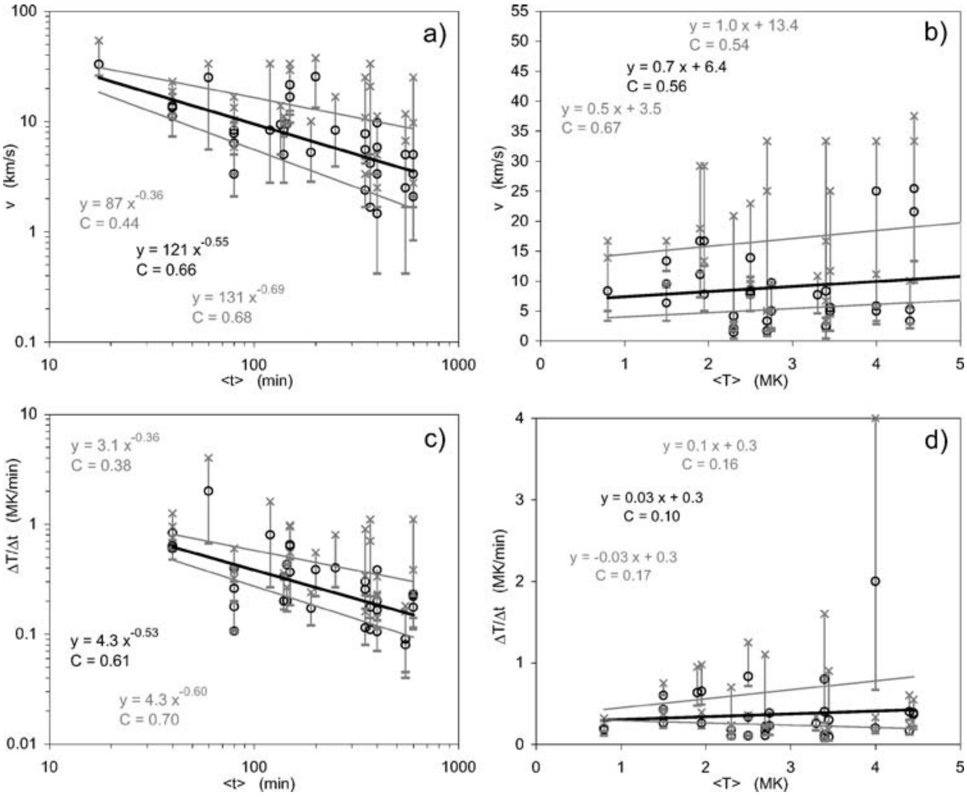

Figure 5. Shrinkage velocity shown as a function of (a) time and (b) temperature. Cooling rate shown as a function of (c) time and (d) temperature. *Circles* represent the "best-overlap" option, whereas *crosses* and *dashes* represent the upper and lower limit estimates, respectively. *Black lines* and *formulae* are least-squares fits for *circles*, and *gray lines* and *formulae* are for *crosses* and *dashes*. Correlation coefficients are denoted as C. Note that in (b) the data point for the transition R25 → R10 lies outside the plotted range of the x-axis ($v = 33\,\mathrm{km\,s^{-1}}$ at $\langle T\rangle = 40\,\mathrm{MK}$).

by circles. The upper limits (crosses) are connected with the lower limits (dashes) by vertical bars. It is important to note that at a particular $\langle t\rangle$ all measurements are given regardless of $\langle T\rangle$. Analogously, all measurements at a particular $\langle T\rangle$ are presented regardless of $\langle t\rangle$. Since v and Q are expected to be functions of $\langle T\rangle$, as well as $\langle t\rangle$, such a coupling could affect the outcome. However, since there is no systematic grouping of measurements at higher/lower temperatures in time, the trends appearing in Figure 5a – d are not directly influenced by such an effect, only the scatter is enlarged. Decoupling of the time/temperature dependence will be presented in Section 4.2.

In Figure 5a, we show the shrinkage velocity as a function of time $\langle t\rangle$, covering more than ten hours of observations (note the log–log scale of the graph). The results reveal that the shrinkage velocity decreases with time: the (mean) shrinkage velocity in the early growth of the flare loop system (some ten minutes after the impulsive

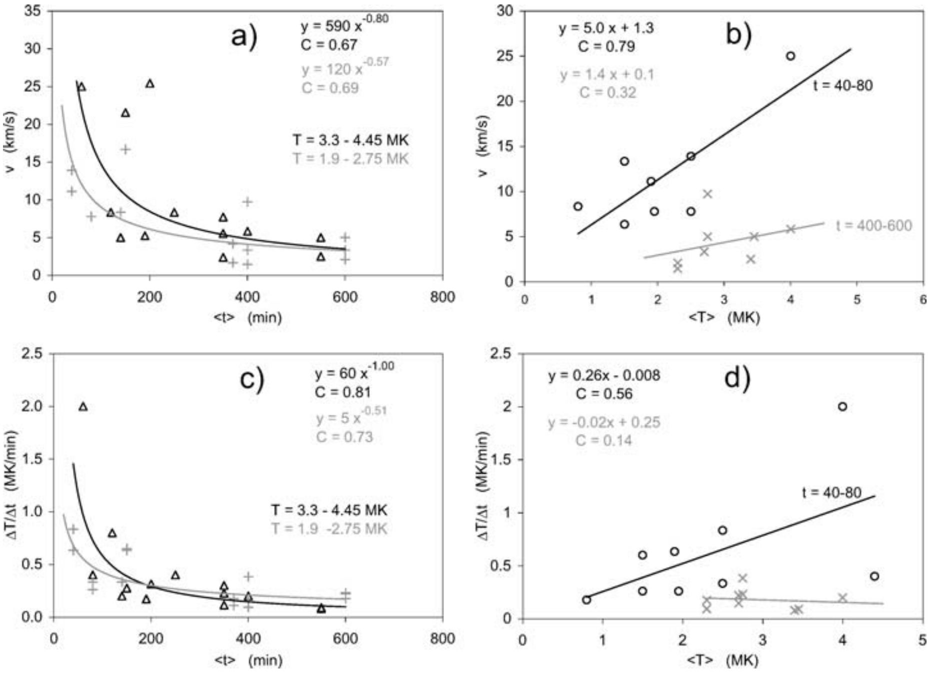

Figure 6. The time/temperature decoupled dependencies based on the "best-overlap" results. Shrinkage velocity (v) is shown as a function of (a) time $\langle t \rangle$, separately for the temperature intervals 3.3 MK $\leq \langle T \rangle \leq$ 4.45 MK (*triangles* and *black* least squares fit) and 1.9 MK $\leq \langle T \rangle \leq$ 2.75 MK (*pluses* and *gray* least squares fit); (b) temperature $\langle T \rangle$, separately for the time intervals 40 minutes $< \langle t \rangle <$ 80 minutes (*circles* and *black* least squares fit) and 400 minutes $< \langle t \rangle <$ 600 minutes (*crosses* and *gray* least squares fit). In (c) and (d) the cooling rate $Q = \Delta T / \Delta t$ is shown as a function of time and temperature in the same manner as v in (a) and (b).

HXR peak) amounts to 30 – 40 km s^{-1} and decreases to a few kilometer per second some ten hours later. Note that the initial shrinkage velocity is comparable to the altitude decrease of the HXR loop-top source at the very beginning of the HXR burst (Veronig *et al.*, 2005).

The data shown in Figure 5a are fitted by the power-law fit $v = a\,(t - t_0)^{-b}$, with fixed $t_0 =$ 09:40 UT. The fit parameters for the "best-overlap" data (circles) are given in the first row of Table I, together with the correlation coefficients, C, and the t-test statistical confidence, P.[3] In Table I we also show the fit with t_0 fixed at 09:50 UT (the impulsive HXR peak).

The power-law fits for the upper-limit and the lower-limit option are shown in Figure 5a by gray lines. From the upper and lower limits one finds that the power-law exponent b ranges between 0.4 and 0.7. Comparing this range with the power-law exponents derived from the "best-overlap" data with t_0 fixed at 09:40

---

[3] For example, $P > 99\%$ means that the probability of no correlation between the two parameters is $P^* = 100 - P < 1\%$.

TABLE I

Parameters of the power-law fits v, $Q = a(t - t_0)^{-b}$ with fixed t_0 = 9:40 and 9:50 UT, obtained using the “best-overlap” data (circles in Figures 5a and c, and 6a and c).

	t_0 = 9:40 UT			t_0 = 9:50 UT		
Parameter	a	b	C [P]	a	b	C [P]
v [all]	121	0.55 ± 0.11	0.66 [>99%]	81	0.49 ± 0.10	0.65 [>99%]
v [3.3 – 4.45 MK]	590	0.80 ± 0.27	0.67 [>98%]	440	0.75 ± 0.25	0.67 [>99%]
v [1.9 – 2.75 MK]	120	0.57 ± 0.16	0.69 [>99%]	90	0.51 ± 0.14	0.68 [>99%]
Q [all]	4	0.53 ± 0.12	0.61 [>99%]	3	0.49 ± 0.11	0.61 [>99%]
Q [3.3 – 4.45 MK]	60	1.00 ± 0.21	0.81 [>99%]	40	0.94 ± 0.19	0.81 [>99%]
Q [1.9 – 2.75 MK]	5	0.51 ± 0.12	0.73 [>99%]	3	0.47 ± 0.11	0.73 [>99%]

The time $t - t_0$ is expressed in minutes, the shrinkage velocity v in kilometer per second, and the cooling rate in MK per minute. We also show the corresponding correlation coefficients C and the statistical significances P derived from the t-test.

TABLE II

Parameters of the linear fits v, $Q = a\,\langle T\rangle + b$ obtained using the “best-overlap” data (circles in Figures 5b and d, and 6b and d).

Parameter	a	b	C	P
v [all]	0.7 ± 0.2	6.4 ± 1.2	0.56	>99%
v [40 – 80 min]	5.0 ± 1.6	1.3 ± 3.6	0.79	>98%
v [400 – 600 min]	1.4 ± 1.6	0.1 ± 4.7	0.32	>60%
Q [all]	0.03 ± 0.06	-0.3 ± 0.2	0.10	>42%
Q [40 – 80 min]	0.26 ± 0.15	-0.01 ± 0.4	0.79	>98%
Q [400 – 600 min]	-0.02 ± 0.06	0.25 ± 0.19	0.14	>38%

The temperature $\langle T\rangle$ is expressed in MK, the shrinkage velocity v in kilometer per second, and the cooling rate Q in MK per minute. The corresponding correlation coefficients C and the statistical significances P derived from the t-test are listed in the fourth and fifth column, respectively.

and 09:50 UT, which give $b \approx 0.55$ and $b \approx 0.49$ (*cf.* Table I), respectively, implies that the choice of t_0 affects the results much less than the measurement errors.

The dependence of the shrinkage velocity on the temperature $\langle T\rangle$ is presented in Figure 5b, using analogous notation as in Figure 5a. Although the scatter is large, the graph shows that the shrinkage velocity is larger at higher temperatures, *i.e.*, when the field lines are closer to the reconnection region. The parameters of the linear-least-squares fits are given in the first row of Table II.

In Figure 5c we present the cooling rate $Q = \Delta T/\Delta t$ as a function of $\langle t\rangle$. The graph shows that the cooling rate decreases with time: the (mean) cooling rate in the early growth of the flare loop system amounts to $\approx$1 MK min^{-1}, whereas some ten hours later the rate becomes about one order of magnitude smaller. The data shown in Figure 5c are fitted by a power-law fit $Q = a\,(t - t_0)^{-b}$, with fixed $t_0 = 09{:}40$ UT. The fit parameters for the "best-overlap" data (circles) are given in the fourth row of Table I, together with those obtained with t_0 fixed at 09:50 UT. In Figure 5c we also show the power-law fits for the upper and lower limits (gray). From that one finds that the power-law exponent ranges between $b \approx 0.4$ and 0.6, implying that the choice of t_0 affects the results much less than the measurement errors.

In Figure 5d, we show the dependence of the cooling rate $Q = \Delta T/\Delta t$ on the temperature $\langle T\rangle$. According to the parameters of the linear fit presented in Table II, the data show no correlation.

4.2. DECOUPLING OF THE TIME AND TEMPERATURE DEPENDENCIES

In this section, we try to decouple the time dependence from the temperature dependence, inherent in the relationships considered in Section 4.1. The outcome for the "best-overlap" data is summarized in Figure 6 and Tables I and II.

The shrinkage velocity is shown as a function of time in Figure 6a, separately for the temperature ranges $1.9\,\mathrm{MK} \le \langle T\rangle \le 2.75\,\mathrm{MK}$ (gray) and $3.3\,\mathrm{MK} \le \langle T\rangle \le 4.45\,\mathrm{MK}$ (black). Figure 6a shows that the shrinkage velocity becomes smaller as the flare decays, and that it is larger at higher temperatures.

The data shown in Figure 6a are fitted by the power-law fit $v = a\,(t - t_0)^{-b}$, with fixed $t_0 = 09{:}40$ UT. The fit parameters for the "best-overlap" data (circles) are given in the second and third rows of Table I, together with the correlation coefficients, C, and the t-test statistical confidence P. In Table I we also list the fit results obtained with t_0 fixed at 09:50 UT (the impulsive HXR peak). One finds that the choice of t_0 affects the power-law exponents less than the data scatter itself.

In Figure 6b the shrinkage velocity is shown as a function of the temperature $\langle T\rangle$ separately for the time intervals 40 minutes $< \langle t\rangle <$ 80 minutes and 400 minutes $< \langle t\rangle <$ 600 minutes. In both intervals, the shrinkage velocity is larger at higher temperatures. On the other hand, the shrinkage is slower in late phases of the flare (second interval), consistent with the results shown in Figure 6a. Furthermore, the slope of the dependence is steeper in the earlier interval, *i.e.*, the shrinkage speed close to the current sheet is considerably larger in the impulsive phase than in the late phases. The superposition of the two phases creates a triangular distribution of the data points, smearing out the correlation in Figure 5b.

The parameters of the linear least squares fits shown in Figure 6b are listed in Table II. The parameters show that in the 40 – 80 minutes interval, the correlation can be expressed as v (km s^{-1}) $\approx 5\langle T\rangle$ (MK). For the 400 – 600 minutes interval one finds v (km s^{-1}) $\approx 1.4\langle T\rangle$ (MK).

The mean shrinkage velocity in the 5 MK temperature range in the early stage amounts to $\approx$25 km s^{-1}, whereas for the transition EIT $\rightarrow$ Hα the mean velocity amounts to $\approx$5 km s^{-1}. In the late stages, the shrinkage velocity in the whole $\langle T \rangle <$ 5 MK range falls below 5 km s^{-1}.

In Figure 6c, we show the cooling rate Q as a function of time, separately for the temperature ranges 1.9 MK $\leq \langle T \rangle \leq$ 2.75 MK (gray) and 3.3 MK $\leq \langle T \rangle \leq$ 4.45 MK (black). From Figure 6c it can be concluded that in the early stages (say, first two hours) the cooling rate is faster at larger temperatures than at lower temperatures, whereas in the late phases it does not depend on the temperature.

The data shown in Figure 6c are fitted by the power-law fit $v = a\,(t - t_0)^{-b}$, with t_0 fixed at 09:40 UT. The fit parameters for the "best-overlap" data (circles) are given in the fifth and sixth rows of Table I, together with the correlation coefficients, C, and the t-test statistical confidence P. In Table I we also show the fit with t_0 fixed at 09:50 UT (the impulsive HXR peak). One finds that the choice of t_0 affects the power-law exponents less than the data scatter itself.

Figure 6d shows that in the early stage ($t = 40 - 80$ minutes, black) the cooling rate is correlated with the temperature, $Q\,(\mathrm{MK\,min}^{-1}) \approx 0.26\langle T \rangle$ (MK) (see fifth row of Table II). The mean cooling rate in the 5 MK temperature range amounts to 1 – 1.5 MK min^{-1}. In the late phases of the event ($t = 400 - 600$ min, gray) we find no correlation (sixth row of Table II), *i.e.*, the cooling rate does not depend on the temperature, which is consistent with Figure 6c. The mean value in the interval 400 – 600 minutes amounts to 0.2 MK min^{-1}. The superposition of the two phases creates a triangular distribution of data points, smearing out the correlation in Figure 5d.

After inspecting the data in more detail, we found that if the data are divided into time bins 40 – 80, 120 – 200, 250 – 370, and 400 – 600 minutes, the average temperature in each bin is approximately the same, $\overline{\langle T \rangle} \approx 3$ MK. That provides another way to represent the time dependence of the shrinkage velocity and the cooling rate, decoupled from the temperature dependence. The outcome is presented in Appendix A.

5. Cooling of Loops

Cooling of flare loops is a complex phenomenon, influenced by a number of effects. The most important processes are conductive and radiative cooling (Culhane, Vesecky, and Phillips, 1970; Švestka, 1987; Culhane *et al.*, 1994), chromospheric "evaporation" (Antiochos and Sturrock, 1978), and betatron heating (Karlický and Kosugi, 2004; Veronig *et al.*, 2005). At high temperatures, the heat is conducted to the transition region and chromosphere, from where it is released by radiation and is partly transformed to kinetic energy of the evaporation flow. When the loop temperature drops below a critical value, which depends on the loop density, the radiative losses from the loop become dominant. In the following, we consider only the basic features of the cooling process, so we utilize the simplified energy equation employed by Švestka (1987):

$$-\frac{\mathrm{d}T}{\mathrm{d}t} = Q_\mathrm{c} + Q_\mathrm{r}, \tag{1}$$

where

$$Q_\mathrm{c} = 2.4 \times 10^{11}\,\frac{T^{7/2}}{n\,L^2} \tag{2}$$

provides an estimate for the conductive cooling rate (for a wider perspective see, *e.g.*, Varady and Heinzel, 1997a,b, and references therein), whereas

$$Q_\mathrm{r} = 2.4 \times 10^{-10}\,\frac{n}{T^{1/2}} \tag{3}$$

is an approximate expression for the radiative cooling rate of optically thin plasma in the range $T > 10^5$ K (*e.g.*, Priest, 1982; Cargill, 1994): Equations (2) and (3) are written in MKS, so the particle density n is expressed in m^{-3} and the loop half-length, $L \approx h\pi/2$, in m, giving Q_c and Q_r in $\mathrm{K\,s^{-1}}$.

Our results concerning the cooling rate show a distinct Q–T correlation in the interval $t = 40-80$ minutes (*cf.*, Figure 6d). A similar correlation can be found by extending the time interval to $t \approx 200$ minutes, but with a decreasing correlation coefficient. For $t > 200$ minutes, we find no correlation between Q and T. Such an outcome indicates that conductive cooling dominates in the early phases of the loop-system growth, but later on radiative cooling becomes more important.

In Figure 7a and 7b we show the measured values of Q (expressed in $\mathrm{MK\,min^{-1}}$) *versus* the parameters $X_\mathrm{c} = n^{-1}\,\langle h\rangle^{-2}\,\langle T\rangle^{7/2}$ in the interval $t = 40-80$ minutes, and $X_\mathrm{r} = n\,\langle T\rangle^{-1/2}$ in the interval $t = 400-600$ minutes, respectively. We estimated n at a given height $\langle h\rangle$ utilizing the five-fold Saito coronal density model (Saito, 1970).

In the interval $t = 40-80$ minutes, we find a distinct correlation $Q = 7.5_{\pm 2.8}\,X_c + 0.3_{\pm 0.2}$ with $C = 0.72$ and $P > 97\%$; *i.e.*, $Q \approx 8X_\mathrm{c}$. The correlation between Q and X_c exists for the data extending up to $t \approx 200$ minutes – considering the time interval $40 \leq t < 200$ one finds $Q = 6_{\pm 2}\,X_c + 0.3_{\pm 0.1}$; $C = 0.60$, $P > 99\%$.[4] On the other hand, we find that Q and X_r are anti-correlated (see inset in Figure 7a). Such a behavior demonstrates that conductive cooling is dominant in the early phase of the loop-system growth, since $Q \sim X_\mathrm{c}$ is consistent with Equation (2), assuming $L \sim \langle h\rangle$. On the other hand, the anti-correlation of Q and X_r contradicts Equation (3) if the radiative cooling would dominate.

On the other hand, the data in the late phase of the loop-system growth indicate an increasing importance of radiative cooling, since a weak correlation between Q and X_r appears (Figure 7b): in the interval $t = 400-600$ minutes one finds $Q = 0.6_{\pm 0.9}\,X_r - 0.009_{\pm 0.26}$ with $C = 0.24$ and $P > 47\%$. On the other hand, no

---

[4] Note that the slope of the correlation and the correlation coefficient are decreasing with increasing t, but the statistical significance increases due to a larger number of data points.

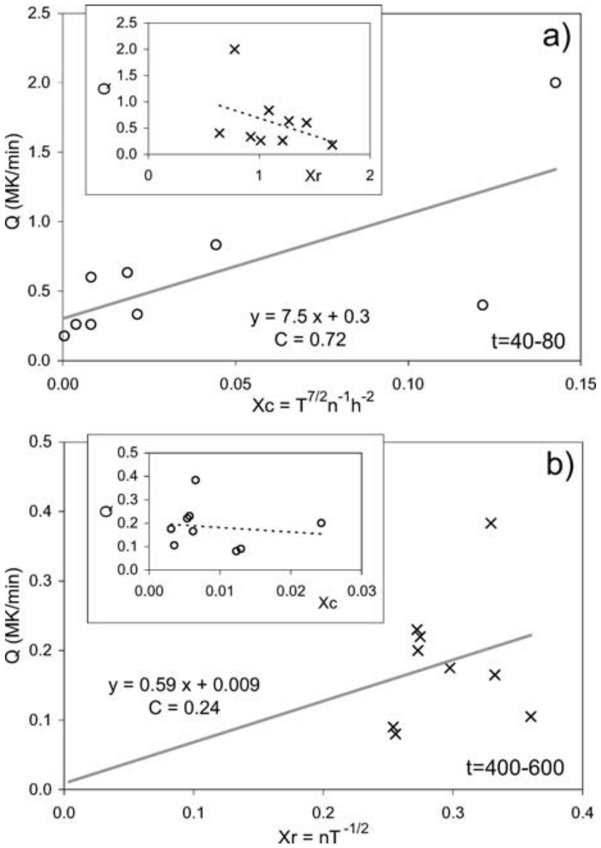

Figure 7. Dependence of the cooling rate $Q = \Delta T/\Delta t$ (expressed in MK per minute) on (a) the parameter $X_{\mathrm{c}} = T^{7/2}n^{-1}h^{-2}$ for the interval $t = 40-80$ minutes (in the inset the dependence on the parameter $X_{\mathrm{r}} = T^{-1/2}n$ is shown); (b) the parameter X_{r} for the interval $t = 400-600$ minutes (in the inset the dependence on the parameter X_{c} is shown). X_{c} and X_{r} are evaluated by expressing T in MK, n in 10^9 cm^{-3}, and h in Mm.

correlation between Q and X_{c} can be found any longer (see inset in Figure 7b). If only the interval $t = 500-600$ minutes is considered, one finds a steeper slope of the Q–X_{r} correlation and a larger statistical significance: $Q = 2.5_{\pm 1.8}\, X_r - 0.5_{\pm 0.5}$ with $C = 0.62$ and $P > 74\%$, but note that the result is based on five data points only.

We repeated the procedure presented in Figure 7 by applying also the 2 – 10-fold Saito model, 1 – 4-fold Newkirk density model (Newkirk, 1961), and the “hybrid” coronal density model (Vršnak, Magdalenić, and Zlobec, 2003), and the outcome was qualitatively the same.

In order to inspect the cooling process more directly, we show in Figure 8 the cooling from $T = 5$ MK to 10^4 K based on the data gathered at $t \approx 80$ minutes: At this time, we can follow the plateau-like feature successively in SXI-b, SXI-o, EIT,

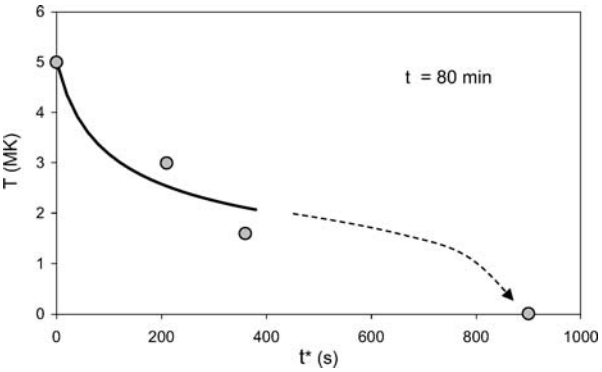

Figure 8. Cooling from $T = 5\,\mathrm{MK}$ to 10^4 K around $t = 80$ minutes; t^* is the time elapsed after the measurement of the hottest source (SXI-b, $T = 5\,\mathrm{MK}$). The *thick line* represents the fit of the form $T = T_1(1 + at^*)^{-2/5}$ for the data $t^* < 400$ seconds. The *thin dashed arrow* (drawn provisionally) outlines cooling from $T = 2\,\mathrm{MK}$ to 10^4 K, the last part depicting radiative losses (the slope becomes steeper at lower temperatures).

and Hα (Figure 2). The time t^* is expressed in seconds relative to the instant of the highest-temperature loop-top measurement (SXI-b, $T = 5\,\mathrm{MK}$).

According to Figure 8, the interval $t^* < 400$ seconds, during which the plasma temperature decreased to $T \approx 2\,\mathrm{MK}$, is most likely dominated by conductive cooling. So, we fitted the $t^* < 400$ seconds measurements by a function of the form $T = T_1(1+at^*)^{-2/5}$, which is the solution of the simple energy equation containing only conductive losses (Culhane *et al.*, 1994; see also Varady and Heinzel, 1997b). Here, T_1 is the temperature at $t^* = 0$, whereas $1/a = \tau_c = 1.2 \times 10^{11}\,\mathrm{n\,k_B\,L^2}\,T_1^{-5/2}$ represents the conductive cooling time from the temperature T_1. The fit gives $T_1 = 5 \pm 0.5\,\mathrm{MK}$ and $a = 0.02 \pm 0.012\,\mathrm{s}^{-1}$.

The outcome shown in Figure 8 can be directly compared with that presented in Figure 11 of Aschwanden and Alexander (2001). The basic difference lies in the fact that cooling of their "average loop" is dominated by radiation already at 20 MK. The conductive cooling lasts for ≈3 minutes, and at 30 MK amounts to about $5\,\mathrm{MK\,min^{-1}}$. In our case, conductive cooling seems to last to below 5 MK, and we find in this range a cooling rate somewhat below $1\,\mathrm{MK\,min^{-1}}$. However, back-extrapolating the fitted curve in our Figure 8 would give values similar to those obtained by Aschwanden and Alexander (2001), or Culhane *et al.* (1994) who found $\approx 10\,\mathrm{MK\,min^{-1}}$ in the 20 MK range and $\approx 1\,\mathrm{MK\,min^{-1}}$ in the 10 MK range (see Figure 15 therein).

On the other hand, the radiative cooling phase found by Aschwanden and Alexander (2001) lasts for seven minutes. In our case, radiative cooling starts in the 2 – 3 MK range and lasts for ten minutes. Note however, that both results are based on only a few data points, and are strongly affected by the data reduction procedure and the measurement accuracy. Consequently, the outcome has to be taken with some caution. Nevertheless, we believe that the difference between our results and the results of Aschwanden and Alexander (2001) is real, most likely due to somewhat larger length of their loops and probably a larger loop density (their analysis includes the impulsive phase of the flare when the evaporation is certainly much more effective than in the post-impulsive main phase of the flare).

6. Discussion and Conclusion

The method presented here provides simultaneous measurement of the shrinkage and cooling of flare loops, unlike previous studies where either shrinking (*e.g.*, Forbes and Acton, 1996; Sheeley, Warren, and Wang, 2004; Li and Gan, 2005) or cooling (*e.g.*, Culhane *et al.*, 1994; Aschwanden and Alexander, 2001) were treated. We briefly summarize the outcome of our analysis as follows:

1. Loop shrinkage is faster at higher temperatures – in the first hour of the loop-system growth the velocity at 5 MK amounts to 20 – 30 km s^{-1}, whereas at 1 MK it is 5 km s^{-1} (*cf.*, Figure 6b);
2. Shrinking slows with time (Figures 5a and 6a, see also Appendix A) – ten hours after the impulsive phase the shrinkage velocity at 5 MK becomes 5 km s^{-1} (Figure 6b);
3. The cooling rate decreases as the flare decays (Figure 6c, see also Appendix A) – in the 5 MK range, in the first hour of the loop-system growth, it amounts to 1 MK min^{-1}, whereas ten hours later it decreases to 0.2 MK min^{-1} ($\approx 20 \times 10^3$ and 3×10^3 K s^{-1}, respectively);
4. During the initial phase of the loop-system growth the cooling rate is larger at higher temperatures (*cf.*, Figure 6d);
5. In the late phases, the obtained values of the cooling rate apparently do not depend on the temperature (Figure 6d).

The described behavior of the loop system can be straightforwardly interpreted in terms of the two-ribbon flare model (*cf.*, Priest, 1982). According to this model, the current sheet is formed in the wake of the expanding CME, and when the CME gets high enough fast reconnection sets in (*e.g.*, Lin and Forbes, 2000). Highly bent reconnected field lines are expelled from the current sheet by the sling-shot effect. In this way, the upward and downward directed hot outflow jets are created, characterized by a flow speed in the order of the Alfvén speed in the external region.[5]

Since our shrinkage velocities are considerably lower than the coronal Alfvén speed, our observations obviously do not include the reconnection outflow itself. Rather, we measured the deflection sheath region below the current sheet

---

[5] More precisely, the outflow speed amounts to $v_{\rm o} = B_{\rm i}(\mu\rho_{\rm o})^{-1/2}$, where $B_{\rm i}$ is the magnetic field in the reconnection–inflow region and $\rho_{\rm o}$ is the density in the reconnection–outflow region; for details see, *e.g.*, Vršnak and Skender (2004).

(Forbes, 1986), where the reconnection jet decelerates as the flow approaches the solar surface and low-lying stationary coronal structures. Deceleration of the flow implies that the shrinkage of the magnetic field-line loops in the deflection sheath is also decelerated.

The plasma confined in the loops that are released from the current sheet is initially hot (for details see, *e.g.*, Vršnak and Skender, 2004). In the course of shrinkage, the plasma cools due to conductive and radiative losses. Since our observations cover only the lower parts of the deflection sheath, the involved temperatures ($T < 5\,\mathrm{MK}$) have to be much lower than in the current sheet itself. The summary item four shows that during the initial phase of the loop-system growth the cooling is mostly governed by the conductive losses, since these are larger at higher temperatures. The summary item five indicates that in the late phases the radiation becomes more important.

In Section five and Appendix B we extended the analysis of shrinking/cooling by considering in more detail an interval approximately one hour after the impulsive phase ($t = 80$ minutes), where a particular feature in the $h(t)$ curves could be identified through several temperature channels. In Section five we showed that conductive cooling probably dominates down to $T \approx 3\,\mathrm{MK}$, whereas radiative cooling becomes dominant below $T \approx 2\,\mathrm{MK}$. A few hours after the impulsive phase, radiative cooling becomes dominant across the whole $T < 5\,\mathrm{MK}$ range. Such a result is qualitatively similar to the result by Culhane *et al.* (1994) and Aschwanden and Alexander (2001), in the sense that conductive cooling dominates at high temperatures. Moreover, the cooling rates we inferred appear to be quantitatively similar to those obtained by Culhane *et al.* (1994) and Aschwanden and Alexander (2001).

In Appendix B we demonstrate that the deceleration of the shrinkage, amounts to $\overline{a} \approx 10\,\mathrm{m\,s^{-2}}$ in the $T < 5\,\mathrm{MK}$ range. Comparing our results with those reported by Forbes and Acton (1996), Sheeley, Warren, and Wang (2004), or Li and Gan (2005) we found a similar amount of shrinking (≈30%), consistent also with the model by Lin (2004). Our results can be most directly compared with those of Sheeley, Warren, and Wang (2004). Although some differences are found (see Appendix B), both results indicate a time-dependent (decreasing) deceleration of the shrinkage.

Acknowledgements

We are grateful to the RHESSI, SOHO, and SXI teams for operating the instruments and performing the basic data reduction, and especially, for the open data policy. We thank Pavol Rapavy and Jan Rybák for providing us with Hα images from the Rimavska Sobota Observatory (Slovakia) and to Z. Švestka for helpful comments. M.T. and A.V. acknowledge the support by the Austrian Science Fund (FWF grant P15344 and J2512-N02). M.K. acknowledges the support by Grant A3003202 of the Academy of Sciences of the Czech Republic.

Appendix A: Shrinking/Cooling at $T \approx 3\,\mathrm{MK}$

If the data are divided into time bins 40 – 80, 120 – 200, 250 – 370, and 400 – 600 min, the average temperatures in the bins turn out to be approximately the same, $\overline{\langle T\rangle} = 2.5$, 2.9, 3.1, and 2.9 MK, respectively, *i.e.*, $\overline{\langle T\rangle} \approx 3\,\mathrm{MK}$. That provides another way to represent the time dependence of the shrinkage velocity and the cooling rate, decoupled from the temperature dependence. The list of measurements is given in Table AI, and the result is shown in Figure A9.

Figure A9a presents the dependence of the bin-averaged shrinkage velocity $\overline{v}$ as a function of time. The horizontal bars depict the time intervals, whereas vertical error bars represent the standard deviation of $\overline{v}$ evaluated for each bin separately. The power-law and linear least-square fits display $\overline{v} = 140\,\overline{\langle t\rangle}^{(-0.56\pm0.19)}$ and $\overline{v} = -0.021_{\pm0.006}\,\overline{\langle t\rangle} + 14_{\pm2}$, with correlation coefficients $C = 0.90$ and 0.93, respectively. According to the power-law fit, the shrinkage velocity (at $\langle T\rangle \approx 3$ MK) in the early stages of the flare loop-system growth amounts to $v \approx 15\,\mathrm{km\,s^{-1}}$, and decreases to a few kilometers per second after $\approx$ ten hours.

In Figure A9b, we show the cooling rate as a function of time. The data show a distinct power-law dependence $\overline{Q} = 8\overline{\langle t\rangle}^{(-0.61\pm0.04)}$. According to the power-law fit, the mean cooling rate at $\langle T\rangle \approx 3\,\mathrm{MK}$ amounts to $Q \approx 1\,\mathrm{MK\,min^{-1}}$ in the early stages of the flare loop-system growth and decreases to $\approx 0.2\,\mathrm{MK\,min^{-1}}$ after $\approx$ ten hours.

TABLE AI

Number of measurements in different channels in four time intervals.

Transition	$\langle T\rangle$ (MK)	40 – 80 minutes	120 – 200 minutes	250 – 370 minutes	400 – 600 minutes
EIT → Hα	0.80	1	1	0	0
SXI-o → Hα	1.50	2	1	0	0
SXI-pt → Hα	1.90	1	1	0	0
SXI-pm → Hα	1.95	2	1	0	0
SXI-o → EIT	2.30	0	0	1	2
SXI-b → Hα	2.50	2	1	0	0
SXI-pt → EIT	2.70	0	0	1	2
SXI-pm → EIT	2.75	0	0	0	2
SXI-b → EIT	3.30	1	0	0	0
SXI-pt → SXI-o	3.40	0	1	2	1
SXI-pm → SXI-o	3.45	0	0	1	1
SXI-b → SXI-o	4.00	1	1	0	1
SXI-b → SXI-pm	4.40	1	1	0	0
SXI-b → SXI-pm	4.45	0	1	0	0

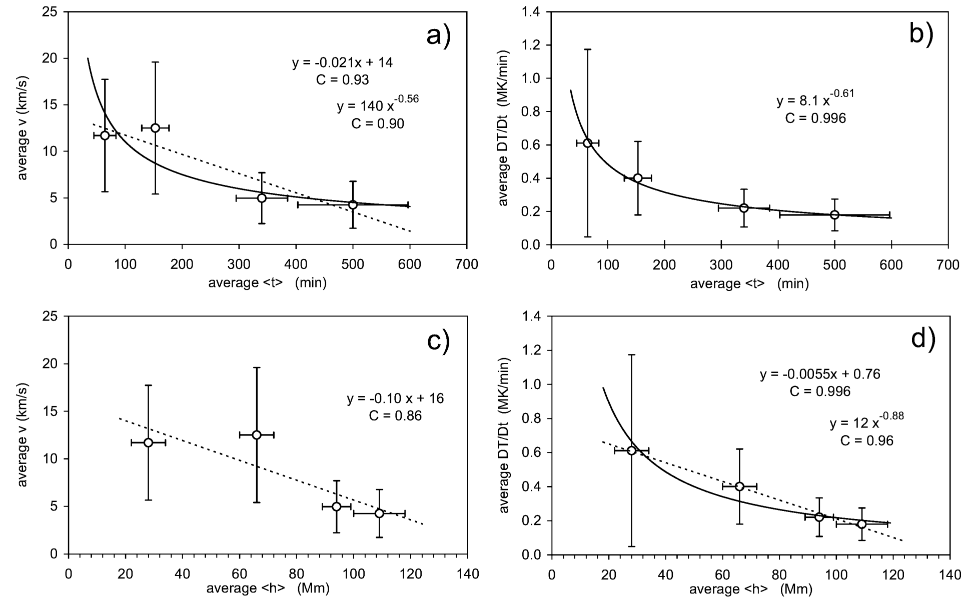

Figure 9. The shrinkage velocity (a) and cooling rate (b) in four time intervals: 40 – 80, 120 – 200, 250 – 370, 400 – 600 minutes. Each bin is characterized by approximately the same bin-average temperature ($\overline{\langle T \rangle} = 2.5, 2.9, 3.1, 2.9$ MK). Vertical error bars are standard deviations, horizontal bars show the duration of time intervals. (c) and (d) Time dependencies transposed to height dependencies: $\langle h \rangle$ represents the height of the loop-top source measured in the SXI-b channel.

In Figure A9c and d we show the shrinkage velocity and the cooling rate as a function of height. The height $\langle h \rangle$ represents the SXI-b loop-top source at the time intervals used in Figure A9a and b.

The results described are consistent with those presented in Section 4.2.

Appendix B: Shrinking at $t = 80$ min

Our results regarding shrinking (Section 4.2) are compatible with the model results presented in Figure 5 of Lin (2004). The higher velocities measured at higher temperatures (Figure 6b) reveal deceleration of shrinking, which is the most prominent feature in Lin's graph. Furthermore, the model predicts lower velocities at later times, which is another straightforward result of our analysis (Figures 5a, 6a, and A9a).

In order to compare more directly our measurements with the results by Lin (2004), we inspected our data to find a situation where a particular feature in the $h(t)$ curves could be identified through several temperature channels. We found such a situation at $\langle t \rangle = 80$ minutes, where we can follow the plateau-like feature successively in SXI-b, SXI-o, EIT, and Hα (Figure 2).

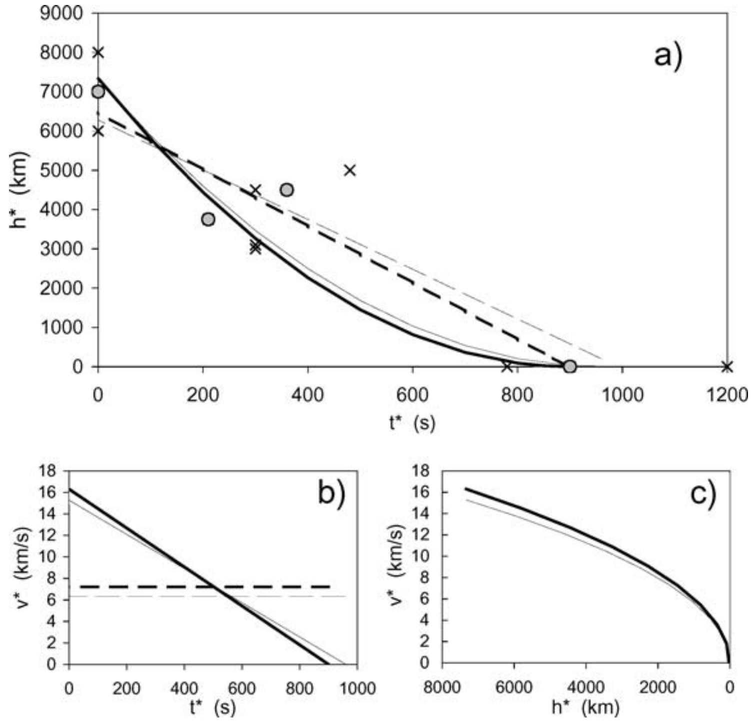

Figure 10. Shrinking at $\langle t \rangle = 80$ min: (a) Height h^* of the sources of different temperatures, measured relative to the Hα loop-top, which was at a height of 23 ± 1 Mm; t^* is the time elapsed after the measurement of the hottest source (SXI-b, $T = 5$ MK). *Circles* and *thick lines* represent the best overlap option, whereas *crosses* represent upper/lower limit options. *Thin lines* represent least squares fits to all data points. Quadratic fits (with fixed $\mathrm{d}h^*/\mathrm{d}t = 0$ at $h^* = 0$) are shown by *solid lines*, the linear fits are drawn by *dashed lines*. Velocities ($v^* = \mathrm{d}h^*/\mathrm{d}t$) obtained from the fits shown in panel a are presented as a function of time and height in panels b and c, respectively.

In Figure A10a we show the shrinkage at $\langle t \rangle = 80$ minutes by including the best overlap data, as well as the upper and lower limit data. The height h^* of the loop-tops of different temperatures is expressed in kilometers relative to the Hα loop-top. The time t^* is expressed in seconds relative to the instant of the highest-temperature loop-top measurement: SXI-b was located 7 ± 1 Mm higher than the corresponding Hα loop-top that appeared 900 s later.

According to Figure A10, the loops shrank from SXI-b to Hα temperatures by $20-25\%$, since the Hα loop height amounted to $h = 23 \pm 1$ Mm at the time considered. Such a shrinkage is comparable with that shown in Figure 5 of Lin (2004). We emphasize that the model predicts a decrease in the amount of shrinking from 43% around 20 minutes after the onset of eruption down to 27% 80 minutes later. Note that the shrinkage we measured covers only the range $T < 5$ MK, *i.e.*, only a part of the shrinking process.

The values we obtained are also similar to those measured by Forbes and Acton (1996), who inferred in two *Yohkoh* events a loop shrinkage of about 20 and 30%. The shrinkage of 30% was also found by Li and Gan (2005) who measured loops observed in microwaves.

Our results can be compared quantitatively with the observations by Sheeley, Warren, and Wang (2004) who followed the loop shrinkage utilizing Transition Region and Coronal Explorer (TRACE) data revealing 10 – 20 MK plasma. The shrinkage velocities we measured in the $T < 5$ MK domain, range from ≈25 to a few kilometer per second, which is considerably slower than the velocities measured by Sheeley, Warren, and Wang (2004), as well as those found by McKenzie (2000), McKenzie and Hudson (1999), and Innes, McKenzie and Wang (2003) who employed *Yohkoh* data. The velocities found by these authors are generally in the range from a hundred to several hundred kilometer per second. The difference is consistent with our interpretation that we measured loop shrinkage in the lower portion of the deflection sheath, since the TRACE and *Yohkoh* data used involve higher temperatures, *i.e.* they characterize the region closer to the current sheet, or possibly even within the current sheet in the case of the fastest downflows (see also Sheeley and Wang, 2002, and the LASCO results in Sheeley, Warren, and Wang, 2004). The shrinkage velocity of $13\,\mathrm{km\,s^{-1}}$ found by Li and Gan (2005), is similar to our speeds, indicating that they also measured lower portions of the deflection sheath.

The data shown in Figure A10a are fitted by a linear as well as a quadratic least squares fit. The linear fit to the best overlap data reads $h^*_{[km]} = -7.2_{\pm 1.5}\,(t^*_{[s]} - 900) - 30_{\pm 970}$ with the correlation coefficient $C = 0.98$ and confidence $P > 95\%$. The fit through all of the data gives $h^* = -6.3_{\pm 1.0}\,(t^* - 900) - 200_{\pm 670}$ with $C = 0.95$ and $P > 99\%$. The quadratic fit is performed by demanding that at $t^* = 900$ s the shrinking stops at $h^* = 0$, *i.e.* $\mathrm{d}h^*/\mathrm{d}t = 0$. The best overlap data give $h^* = -0.009_{\pm 0.001}\,(t^* - 900)^2$ with $C = 0.92$, whereas for all data the fit yields $h^* = -0.008_{\pm 0.001}\,(t^* - 900)^2$ with $C = 0.88$. In Figure A10b and c, we show the velocities defined by the described fits.

A more detailed comparison of the results shown in Figure A10 with the results of Sheeley, Warren, and Wang (2004) shows further differences. The deceleration we get, $\approx 10\,\mathrm{m\,s^{-2}}$, is much smaller than that found by Sheeley, Warren, and Wang (2004) ranging from several hundreds to over thousand meters per square second. Inspecting the data in Figure A10a one finds that the measurement errors cannot account for such a difference. A more likely explanation is that the deceleration is not constant but decreases in time. Another difference concerns our velocities measured around 5 MK, which are higher than the speeds of $4 - 5\,\mathrm{km\,s^{-1}}$ reported by Sheeley, Warren, and Wang (2004) for the end of the deceleration stage, still within the 10 – 20 MK range.

Unfortunately, Sheeley, Warren, and Wang (2004) did not present graphically the $h(t)$ measurements and the corresponding fits, so it is difficult to draw a definite conclusion about the differences. However, inspecting in more detail Figure 3 of

Sheeley, Warren, and Wang (2004), one finds a shrinking velocity of $\approx$7 km s^{-1} at the end of the Fe XXIV 192 Å emission (10 – 20 MK), decreasing to $\approx$3 km s^{-1} at Fe XII 195 Å (1.6 MK) some 10 – 20 minutes later. This gives a deceleration between 3 and 6 m s^{-2}. Such velocities and the corresponding deceleration are quite close to our values, especially bearing in mind the measurement accuracy. Nevertheless, the comparison presented indicates that details of the shrinking kinematics might differ from one event to another, as well as in different stages of the loop-system evolution.

Finally, let us note that our result regarding the shrinkage of the RHESSI loop-top sources might look somewhat puzzling, since the corresponding velocities are much lower than expected for the top of the deflection sheath. However, one should bear in mind that in this stage of the energy release, the heating associated with the betatron acceleration in the collapsing magnetic field (Karlický and Kosugi, 2004; Karlický, Veronig, and Vršnak, 2005) might confuse measurements of the shrinkage velocity, *i.e.* the measurements can result in false speeds (see Section 5.1 of Veronig *et al.*, 2005). Another possibility is that in the early stage of the energy release, the upper part of the deflection sheath is still hotter and at a larger height than the observed RHESSI loop-top sources, so that we observed an intermediate/lower part of the deflection sheath again.

References

Antiochos, S.K. and Sturrock, P.A.: 1978, *Astrophys. J.* **220**, 1137.

Aschwanden, M.J. and Alexander, D.: 2001, *Solar Phys.* **204**, 93.

Cargill, P.J.: 1994, *Astrophys. J.* **422**, 381.

Culhane, J.L., Vesecky, J.F., and Phillips, K.J.H.: 1970, *Solar Phys.* **15**, 394.

Culhane, J.L., Phillips, A.T., Inda-Koide, M., *et al.*: 1994, *Solar Phys.* **153**, 307.

Dauphin, C., Vilmer., N., Lüthi, T., Trottet, G., Krucker, S., and Magun, A.: 2005, *Adv. Space Res.* **35**, 1805.

Delaboudinière, J.-P.: Artzner, G.E.; Brunaud, J., *et al.*: 1995, *Solar Phys.* **162**, 291.

Dowdy, J.F., Jr., Moore, R.L., and Wu, S.T.: 1985, *Solar Phys.* **99**, 79.

Forbes, T.G.: 1986, *Astrophys. J.* **305**, 553.

Forbes, T.G. and Acton, L.W.: 1996, *Astrophys. J.* **459**, 330.

Furth, H.P., Kileen, J., and Rosenbluth, M.N.: 1963, *Phys. Fluids* **6**, 459.

Gekelman, W. and Pfister, H.: 1988, *Phys. Fluids* **26**, 1949.

Heinzel, P. and Karlický, M.: 1987, *Solar Phys.* **110**, 343.

Hiei, E.: 1994, in V. Sušin, P. Heinzel, and J.-C. Vial (eds.), *IAU Colloq., Solar Coronal Structures* **144**, 163.

Hill, S.M., Pizzo, V.J., Balch, C.C., Biesecker, D.A., Bornmann, P. Hildner, E., *et al.*: 2005, *Solar Phys.* **226**, 255.

Hurford, G.J., Schmahl, E.J., Schwartz, R.A, *et al.*: 2002, *Solar Phys.* **210**, 61.

Innes, D.E., McKenzie, D.E., and Wang, T.: 2003, *Solar Phys.* **217**, 267.

Karlický, M. and Kosugi, T.: 2004, *Astron. Astrophys.* **419**, 1159.

Karlický, M., Veronig, A., and Vršnak, B.: 2005, *Hvar Observ. Bull.*, in press.

Ko, Y., Raymond, J.C., Lin, J., Lawrence, G., Li, J., and Fludra, A.: 2003, *Astrophys. J.* **594**, 1068.

Li, Y.P. and Gan, W.Q.: 2005, *Astrophys. J.* **629**, L137.

Lin, J.: 2004, *Solar Phys.* **222**, 115.

Lin, J. and Forbes, T.G.: 2000, *J. Geophys. Res.* **105**, 2375.

Lin, J., Forbes, T.G., Priest, E.R., and Bungey, T.N.: 1995, *Solar Phys.* **159**, 275.

Lin, J., Ko, Y.-K., Sui, L., *et al.*: 2005, *Astrophys. J.* **622**, 1251.

Lin, R.P., Dennis, B.R., Hurford, G.J., *et al.*: 2002, *Solar Phys.* **210**, 3.

Lin, R.P., Schwartz, R.A., Pelling, R.M., and Hurley, K.C.: 1981, *Astrophys. J.* **251**, L109.

Liu, W., Jiang, Y.W., Liu, S., and Petrosian, V.: 2004, *Astrophys. J.* **611**, L43.

McKenzie, D.E.: 2000, *Solar Phys.* **195**, 381.

McKenzie, D.E. and Hudson, H.S.: 1999, *Astrophys. J.* **519**, L93.

Newkirk, G., Jr.: 1961, *Astrophys. J.* **133**, 983.

Otruba, W.: 1999, in B. Schmieder, A. Hofmann, and J. Staude (eds.), *Third Advances in Solar Physics Euroconference: Magnetic Fields and Oscillations*, ASP Conference Series, Vol. 184, p. 314.

Otruba, W. and Pötzi, W.: 2003, *Hvar Observ. Bull.* **27**, 189.

Pizzo, V.J., Hill, S.M., Balch, C.C., Biesecker, D.A., Bornmann, P., Hildner, E., *et al.*: 2005, *Solar Phys.* **226**, 283

Priest, E.R.: 1982, *Solar Magnetohydrodynamics*, D. Reidel, Dordrecht.

Saito, K: 1970, *Ann. Tokyo Astr. Obs.* **12**, 53.

Schmieder, B., Heinzel, P., Van Driel-Gesztelyi, L., and Lemen, J.R.: 1996, *Solar Phys.* **165**, 303.

Sheeley, N.R., Jr. and Wang, Y.-M.: 2002, *Astrophys. J.* **579**, 874.

Sheeley, N.R., Jr., Warren, H.P., and Wang, Y.-M.: 2004, *Astrophys. J.* **616**, 1224.

Švestka, Z.: 1976, *Solar Flares*, Reidel, Dordrecht.

Švestka, Z.: 1986, in D. Neidig (ed.), *Proceedings of the NSO/SMM Symposium on the Lower Atmosphere of Solar Flares*, p. 332.

Švestka, Z.: 1987, *Solar Phys.* **108**, 411.

Švestka, Z., Fontenla, J.M., Machado, M.E., Martin, S.F., Neidig, D.F., and Poletto, G.: 1987, *Solar Phys.* **108**, 237.

Ugai, M.: 1987, *Geophys. Res. Lett.* **14**, 103.

Van Driel-Gesztelyi, L., Schmieder, B., Wiik, J.-E., *et al.*: 1996, in R.D. Bentley and J.T. Mariska (eds.), *Magnetic Reconnection in the Solar Atmosphere*, ASP Conference Series, Vol. 111, p. 359.

Varady, M. and Heinzel, P.: 1997a, *Hvar Observ. Bull.* **21**, 33.

Varady, M. and Heinzel, P.: 1997b, in A. Wilson (ed.), *Fifth SOHO Workshop: The Corona and Solar Wind Near Minimum Activity*, ESA-SP404, pr 705.

Veronig, A., Karlický, M., Vršnak, B., Temmer, M., Magdalenić, J., Dennis, B.R., Otruba, W., and Pötzi, W.: 2005, *Astron. Astrophys.* **446**, 675.

Vršnak, B. and Skender, M.: 2004, *Solar Phys.* **226**, 97.

Vršnak, B., Klein, K.-L., Warmuth, A., Otruba, W., and Skender, M.: 2003, *Solar Phys.* **214**, 325.

Vršnak, B., Magdalenić, J., and Zlobec, P.: 2003, *Astron. Astrophys.* **413**, 753.

Vršnak, B., Magdalenić, J., Temmer, M., Veronig, A., Warmuth, A., Mann, G., Aurass, H., and Otruba, W.: 2005, *Astrophys. J.* **625**, L67.

Vršnak, B., Warmuth, A., Temmer M., Veronig, A., Magdalenić, J., Hillaris, A., and Karlický, M.: 2006, *Astron. Astrophys.*, in press.

Webb, D.F., Burkepile, J., Forbes, T.G., and Riley, P.: 2003, *J. Geophys. Res.* **108**, 1440.